Thermoelectric transport of a topological semimetal with a pair of Weyl points and a nodal ring in the quantum limit

L. W. Guo and C. M. Wang ●*

Department of Physics, Shanghai Normal University, Shanghai 200234, China

We explore the thermoelectric transport properties of a coexistence topological semimetal, characterized by the presence of both a pair of Weyl points and a nodal ring in the quantum limit. This system gives rise to complex Landau bands when subjected to a magnetic field aligned with the direction connecting two Weyl points. In the longitudinal configuration, where the magnetic field is parallel to the electric field or the temperature gradient, the thermoelectric conductivity indicates a plateau independent of the magnetic field and the Fermi energy at δ-form short-range scattering. This platform structure should also exist in pure two-node Weyl semimetals. However, the thermoelectric conductivity and the Seebeck coefficient are significantly influenced by the parameters of long-ranged Gaussian or screened Coulomb scattering potentials for both fixed carrier density and Fermi energy scenarios. In the transverse configuration, both Gaussian and screened Coulomb scatterings yield substantial positive magnetoresistance and thermoelectric conductance. Since the Hall conductivity is larger than the longitudinal one, the Seebeck coefficient, exhibiting a quadratic increase with the magnetic field, is close to the dissipationless limit irrespective of scatterings, while the Nernst response is notably dependent on the scattering mechanism. Additionally, the model parameter, distinct from the two-node Weyl model, influences the thermoelectric transport properties. The magnetic field response of the thermoelectric coefficients to different scattering potentials can be used as a basis for distinguishing scattering mechanisms in materials.

I. INTRODUCTION

Topological semimetals [1–7] have recently attracted increasing attention due to their nontrivial and exotic physical phenomena: their band structure includes symmetry-protected band crossings between the valence and conduction bands, and they exhibit unconventional responses to applied external fields [8–13]. In particular, as thermoelectric effects are proportional to the derivative of conductivity, they are generally considered more sensitive to these novel responses [14–21]. In recent years, theoretical studies of three-dimensional Dirac/Weyl semimetals in the quantum limit, where only the lowest Landau band is occupied by electrons, have shown that the Seebeck coefficient S_{xx} indicates an unsaturated linear growth at low temperatures [22]. Further investigation demonstrated that the linear growth of the Seebeck coefficient in the clean limit originates from the the plateau value of thermoelectric Hall conductivity α_{xy} [23,24], proportional to the temperature. The plateau of α_{xy} or the equivalent linear growth of S_{xx}, recognized as a signature of topological semimetals, has been observed in the Dirac semimetal ZrTe$_5$ [25,26], Pb$_{1-x}$Sn$_x$Se [14], the Weyl semimetal TaP [27], and nodal-line semimetal graphite [28,29]. Hence, topological semimetals show great potential in the realm of thermoelectric transport.

Recently, a distinctive class of topological states, termed "topological coexistence," has been identified in certain topological materials [30–37]. Diverging from traditional topological semimetals characterized by a single topological state, these materials showcase the simultaneous presence of multiple topological states in the bulk. One notable example is found in the double perovskites Ba$_2$CdReO$_6$ [30], which host both Weyl and nodal ring topological states. In a related study, Zhang *et al.* [31] investigated the surface states of the ferromagnetic material Cs$_2$MoCl$_6$, sharing the same space group $Fm\bar{3}m$ as Ba$_2$CdReO$_6$ and featuring analogous topological coexistence states. Their findings reveal a unique surface state connection between Weyl and nodal ring fermions, a phenomenon also predicted in other systems [33,34]. In these materials, spin-orbit coupling plays a key role in the formation of a coexisting topological state.

Topological coexisting materials, as a new class of topological phases, have energy bands that are quite different from those previously studied, which may bring special thermoelectric transport properties. In the quantum limit, there is only one energy band that contributes to transport. At this point, scattering may play a crucial role [38–44]. Our study starts from a two-band model containing both a pair of Weyl points and a nodal ring, and we investigate the longitudinal as well as transverse thermoelectric transport properties in the quantum limit when the magnetic field is applied along the connection of Weyl points by considering both the Gaussian and screened Coulomb electron-impurity scatterings.

II. HAMILTONIAN AND THE LANDAU BANDS

We consider a topological semimetal, where a pair of Weyl nodes and a nodal line coexist. The minimal Hamiltonian is

---

*Contact author: wangcm@shnu.edu.cn

(a) Bulk bands crossing
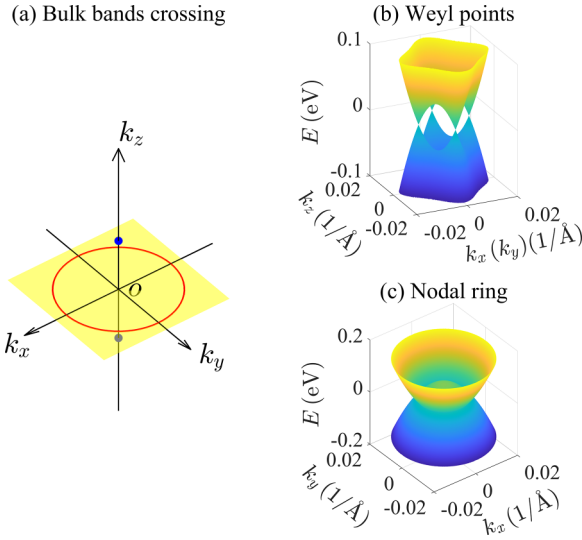

(b) Weyl points

(c) Nodal ring

FIG. 1. (a) The schematic diagram of the band crossing in momentum space, which forms a pair of Weyl points (blue and gray dots) and a nodal ring (red circle). The yellow plane represents the $k_z = 0$ plane. Energy dispersions in the k_x-k_z or k_y-k_z plane (b) and the k_x-k_y plane (c). Here $M_0 = 0.05$ eV, $M_1 = 5$ eV nm^2, and $D = 2M_1$.

written as [31]

$$H = Dk_z(k_x\sigma_x + k_y\sigma_y) + M_{\bm{k}}\sigma_z, \tag{1}$$

with

$$M_{\bm{k}} = M_0 - M_1(k_x^2 + k_y^2 + k_z^2). \tag{2}$$

Here D, M_0, and M_1 are material parameters, $\bm{\sigma} = (\sigma_x, \sigma_y, \sigma_z)$ are three 2×2 Pauli matrices, and $\bm{k} = (k_x, k_y, k_z)$ is the wave vector. The dispersion of the system is

$$E_{\lambda\bm{k}} = \lambda\sqrt{D^2k_z^2(k_x^2 + k_y^2) + M_{\bm{k}}^2}. \tag{3}$$

The quantum number $\lambda = \pm 1$ denotes the conduction and valence bands. Compared to the minimal two-node Weyl semimetal model [45] $H_W = A(k_x\sigma_x + k_y\sigma_y) + M_{\bm{k}}\sigma_z$, the constant Fermi velocity A becomes a momentum-dependent quantity Dk_z, which results in the coexistence of two types of topological states. Two bands contact each other at a pair of Weyl points $(0, 0, \pm\sqrt{M_0/M_1} = \pm k_W)$ on the k_z axis, in addition to a closed nodal line (nodal ring) in the k_x-k_y plane $(k_z = 0, k_x^2 + k_y^2 = k_W^2)$, displaying two topological properties in one system. Figure 1(a) schematically shows the characteristics of band crossing formed by two energy bands of the model, where blue and gray dots represent a pair of Weyl points on the k_z axis, and the red circle represents the nodal ring in the k_x-k_y plane. The panel (b) shows the energy dispersion on the k_x-k_z or k_y-k_z plane, where two additional Weyl points come from the intersections of the ring and the k_x or k_y axis. The panel (c) indicates the dispersion in the $k_z = 0$ plane, where the touch points compose a closed circle.

The Berry curvature is considered to be an important quantity reflecting the topological properties of matter. It can be thought of as the magnetic field in momentum space and is associated with various topological transport responses such as the anomalous Hall effect, the quantum Hall effect, and the

chiral anomaly. Three components of the Berry curvature for the coexistence model are derived in Appendix, and they can be found as

$$\Omega_+^x = \frac{D^2}{2E_+^3}k_zk_x[M_0 - M_1(k_x^2 + k_y^2 - k_z^2)], \tag{4}$$

$$\Omega_+^y = \frac{D^2}{2E_+^3}k_zk_y[M_0 - M_1(k_x^2 + k_y^2 - k_z^2)], \tag{5}$$

$$\Omega_+^z = -\frac{D^2}{2E_+^3}k_z^2[M_0 + M_1(k_x^2 + k_y^2 - k_z^2)]. \tag{6}$$

Here the "+" subscript represents the Berry curvature of the $\lambda = +1$ band. In contrast to the two-node Weyl semimetal [45], three components of the Berry curvature all take zero in the $k_z = 0$ plane. By calculating the integral of the Berry curvature around the Fermi surface near the $\pm k_W$ point, we can obtain a topological charge $n = \pm 1$, corresponding to a pair of Weyl points with opposite chiralities. In addition, we can define a Chern number to determine the topological properties on the k_x-k_y plane. For a given k_z, we can compute the Chern number $n_c(k_z) = -\frac{1}{2\pi}\iint dk_xdk_y\Omega_+^z$ along the z direction. We find for $-k_W < k_z < 0$ or $0 < k_z < k_W$ the Chern number $n_c = 1$, while for the other case $k_z \neq 0$, $n_c(k_z) = 0$. Such a nonzero Chern number corresponds to a k_z-dependent edge state.

Now we apply an external magnetic field in the z-direction $\bm{B} = B\hat{z}$ to the coexisting topological system. The momentum plane perpendicular to the magnetic field will be quantized, while the momentum along the direction of the field is still a good quantum number. In the presence of a magnetic field, the new Hamiltonian could be obtained via the Peierls substitution $\bm{k} \rightarrow \bm{k} - e\bm{A}/\hbar$, with e being the charge of an electron. If we choose the Landau gauge $\bm{A} = -By\hat{x}$, the new Hamiltonian of the coexisting system is shown as the following form:

$$H = \begin{bmatrix} M_0 - M_1(\hat{k}_x^2 + \hat{k}_y^2 + k_z^2) & Dk_z(\hat{k}_x - i\hat{k}_y) \\ Dk_z(\hat{k}_x + i\hat{k}_y) & -M_0 + M_1(\hat{k}_x^2 + \hat{k}_y^2 + k_z^2) \end{bmatrix}, \tag{7}$$

with $\hat{k}_x = k_x - y/\ell_B^2$, $\hat{k}_y = -i\partial_y$, and $\ell_B = \sqrt{\hbar/|eB|}$ being the magnetic length. We can introduce two ladder operators $a^\dagger = (\ell_B/\sqrt{2})(k_x - y/\ell_B^2 + \partial_y)$ and $a = (\ell_B/\sqrt{2})(k_x - y/\ell_B^2 - \partial_y)$, which satisfy $[a, a^\dagger] = 1$. This Hamiltonian is then rewritten as

$$H = \begin{bmatrix} -M_{k_z} - \omega_c(a^\dagger a + \frac{1}{2}) & \omega_z a \\ \omega_z a^\dagger & M_{k_z} + \omega_c(a^\dagger a + \frac{1}{2}) \end{bmatrix}, \tag{8}$$

with the frequencies $\omega_c = 2M_1/\ell_B^2$ and $\omega_z = \sqrt{2}Dk_z/\ell_B$, and $M_{k_z} = -M_0 + M_1k_z^2$. Therefore, the Landau energies and wave functions of the Hamiltonian H for the index $\nu \geqslant 1$ are

$$E_{\lambda\nu} = \frac{1}{2}\omega_c + \lambda\sqrt{[M_0 - M_1k_z^2 - \nu\omega_c]^2 + \nu\omega_z^2}, \tag{9}$$

$$\psi_{+\nu} = \frac{e^{i(k_xx+k_zz)}}{\sqrt{L_xL_z}}\begin{bmatrix} \sin\frac{\alpha_\nu}{2}\phi_{\nu-1} \\ \cos\frac{\alpha_\nu}{2}\phi_\nu \end{bmatrix}, \tag{10}$$

$$\psi_{-\nu} = \frac{e^{i(k_xx+k_zz)}}{\sqrt{L_xL_z}}\begin{bmatrix} \cos\frac{\alpha_\nu}{2}\phi_{\nu-1} \\ -\sin\frac{\alpha_\nu}{2}\phi_\nu \end{bmatrix}, \tag{11}$$
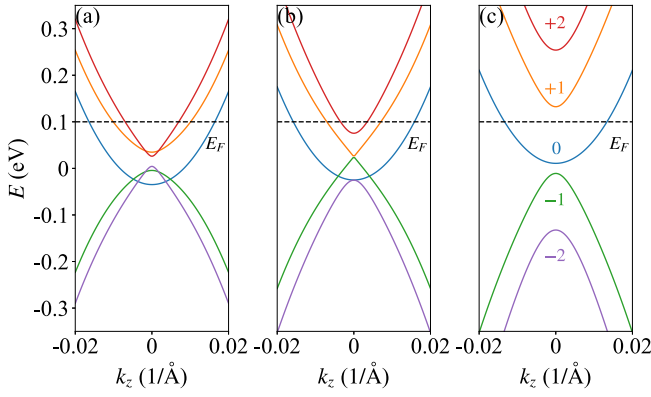
FIG. 2. The Landau energy bands of the system with indices $\nu = 0, 1, 2$ for three different magnetic fields $B = 2, 3.3, 8$ T corresponding to (a), (b), and (c), respectively. Here $M_0 = 0.05$ eV, $M_1 = 5$ eV nm^2, and $D = 2M_1$.

while for $\nu = 0$,

$$E_0 = -M_0 + M_1 k_z^2 + \frac{1}{2}\omega_c, \tag{12}$$

$$\psi_0 = \frac{e^{i(k_x x + k_z z)}}{\sqrt{L_x L_z}} \begin{bmatrix} 0 \\ \phi_0 \end{bmatrix}. \tag{13}$$

Here $L_x L_z$ is the area of the sample and $\tan\alpha_\nu = \sqrt{\nu}\omega_z/(\nu\omega_c + M_{k_z})$. ϕ_ν is the usual harmonic-oscillator eigenstate at the center $y_0 = k_x \ell_B^2$ relating to the Hermite polynomials $\mathcal{H}_\nu(x)$,

$$\phi_\nu(k_x, y) = \frac{1}{\sqrt{\sqrt{\pi}2^\nu \nu! \ell_B}} e^{-[(y-y_0)^2/2\ell_B^2]} \mathcal{H}_\nu\left(\frac{y-y_0}{\ell_B}\right). \tag{14}$$

In contrast to the two-node Weyl semimetal model, there is an additional frequency ω_z in the Landau bands. It relates to the parameter D and is k_z-dependent, which is a key feature of the coexisting system. For the indices $\nu \geqslant 1$, two Landau energy levels $E_{\pm\nu}$ intersect at $k_z = 0$ when the magnetic field $B_\nu = \hbar M_0/(2\nu|e|M_1)$. Figure 2(b) indicates the Landau bands at $B = B_1 \simeq 3.3$ T, where the $+1$ band and the -1 band come into contact at $k_z = 0$. This intersection is a feature of Landau levels in nodal-line semimetals in the presence of the magnetic field perpendicular to the nodal-line plane [46]. But the zeroth Landau energy band E_0 is analogous to the two-node Weyl semimetal model [45], which is quadratic along the k_z direction.

Due to the k_z-dependent frequency ω_z, the Landau bands exhibit a complexity in vivid contrast to the two-node Weyl model, especially at low magnetic fields. In the two-node Weyl model, Landau bands are distinctly separated and organized in the order of band indices [45]. However, in this coexisting topological system, the Landau bands overlap, with even the lowest Landau band extending into the negative band (valence band) at low magnetic fields, as illustrated in Figs. 2(a) and 2(b). This band-crossing behavior is anticipated to give rise to unique magnetic transport phenomena, such as novel magnetoresistance oscillations [47]. Currently, our focus remains on the quantum limit, where only one Landau band is occupied. Fortunately, when the magnetic field is sufficiently large such that the bottom of the zeroth Landau

band is higher than the top of the -1 Landau band, as depicted in Fig. 2(c), the bands become well-separated and ordered according to the Landau indices. This condition occurs when the magnetic field $B > \hbar M_0/(|e|M_1)$, twice the value of B_1. In such cases, if the Fermi energy E_F intersects only the zeroth band, the coexisting topological system enters the quantum limit. Our subsequent calculations will focus on this extreme regime.

III. LONGITUDINAL CONFIGURATION

At first, we consider the longitudinal configuration, where the magnetic field, the electric field, and the temperature gradient are all along the z-direction, $\boldsymbol{B} \parallel \boldsymbol{E} \parallel \boldsymbol{\nabla}T \parallel \hat{z}$. The Mott relation is believed to be valid at temperatures close to 0 K [42]. Hence, in this configuration we only need to calculate the longitudinal conductivity σ_{zz}. The resistivity ρ_{zz} is just the reciprocal of the conductivity, $\rho_{zz} = 1/\sigma_{zz}$. And the thermoelectric Seebeck coefficient S_{zz} could be obtained from the conductivity via the Mott relation [42,48–50]

$$S_{zz} = \frac{\pi^2 k_B^2 T}{3e} \frac{1}{\sigma_{zz}} \frac{\partial \sigma_{zz}}{\partial E_F}. \tag{15}$$

Here k_B is the Boltzmann constant, T is the temperature, and E_F is the Fermi energy.

The longitudinal conductivity σ_{zz} can be expressed as [38,42,44,45]

$$\sigma_{zz} = \frac{\hbar e^2}{2\pi V} \int_{-\infty}^{\infty} d\varepsilon \left[-\frac{\partial n_F(\varepsilon)}{\partial \varepsilon}\right] \text{Tr}[\hat{v}_z \hat{G}^A(\varepsilon)\hat{v}_z \hat{G}^R(\varepsilon)]. \tag{16}$$

Here V is the volume, $n_F(\varepsilon)$ is the Fermi-Dirac distribution function, $\hat{G}^{R/A}(\varepsilon)$ is the retarded (advanced) Green's function, and $\hat{v}_z$ is the z-component of the velocity operator with the form

$$\hat{v}_z = \frac{1}{\hbar}\frac{\partial H}{\partial k_z} = \frac{1}{\hbar}\begin{bmatrix} -2M_1 k_z & \frac{\sqrt{2}}{\ell_B}Da \\ \frac{\sqrt{2}}{\ell_B}Da^\dagger & 2M_1 k_z \end{bmatrix}. \tag{17}$$

Different from the two-node Weyl model, the off-diagonal element of the velocity operator $\hat{v}_z$ is nonzero due to the Dk_z term in the Hamiltonian. However, for any band with nonzero index ν, $\langle\psi_0|\hat{v}_z|\psi_{\pm\nu}\rangle = 0$. Thus in the quantum limit, where the Fermi energy only cuts the lowest Landau band E_0, only the zeroth band E_0 contributes to the conductivity in the longitudinal configuration. In this case, only the velocity element $v_{k_z} = \langle\psi_0|\hat{v}_z|\psi_0\rangle = 2M_1 k_z/\hbar$ involves in the expression leading to the longitudinal conductivity of this coexistence model analogous to the two-node Weyl model [44,45]:

$$\sigma_{zz} = 2\frac{e^2}{h}N_L v_{k_F}\tau_{\text{tr}}^0, \tag{18}$$

where the Landau degeneracy $N_L = 1/2\pi\ell_B^2$, the Fermi group velocity $v_{k_F} = 2M_1 k_F/\hbar$, and the Fermi wave vector k_F is the positive intersection of the Fermi energy and the zeroth Landau band. The transport time at the Fermi energy, denoted as τ_{tr}^0, includes an additional factor $(1 - v_{k_z'}^z/v_{k_F}^z)$ from the vertex correction in its expression, distinct from the particle lifetime [42,51]. This factor introduces a selection rule, allowing only $k_z' = -k_F$ to contribute to the transport time. Finally, τ_{tr}^0 has

the form

$$\frac{\hbar}{\tau_{\text{tr}}^0} = \frac{n_i}{M_1 k_F} \sum_{k_x', \boldsymbol{q}} |u(\boldsymbol{q})|^2 e^{-\frac{q_\parallel^2 \ell_B^2}{2}} \delta_{q_x, k_x - k_x'} \delta_{q_z, 2k_F}. \quad (19)$$

Here n_i is the impurity density, $u(\boldsymbol{q})$ represents the Fourier transform of the scattering potential, the wave vector $\boldsymbol{q} = (q_x, q_y, q_z)$, and $q_\parallel^2 = q_x^2 + q_y^2$.

We consider two popular types of elastic electron-impurity scatterings: the Gaussian potential and the screened Coulomb potential. The former characterizes scenarios where scattering intensity diminishes rapidly with distance from the scattering center, while the screened Coulomb potential represents situations where charged impurities induce substantial screening effects. The Fourier transform of the Gaussian potential is $u(\boldsymbol{q}) = u_0 e^{-q^2 d^2/2}$, where u_0 measures the scattering strength, and d is a parameter that describes the range of the scattering potential. If we define $V_G = n_i u_0^2$, then the transport time is

$$\frac{\hbar}{\tau_{\text{tr}}^{0,G}} = \frac{V_G}{2\pi M_1 k_F (2d^2 + \ell_B^2)} e^{-4k_F^2 d^2}. \quad (20)$$

Therefore, the conductivity has the form

$$\sigma_{zz} = \frac{e^2}{h} \frac{(2M_1 k_F)^2}{V_G} \left(1 + \frac{2d^2}{\ell_B^2}\right) e^{4k_F^2 d^2}. \quad (21)$$

Since only k_F depends on the Fermi energy, the Seebeck coefficient S_{zz} is given by

$$S_{zz} = \frac{\pi^2 k_B^2 T}{3e} \frac{1}{M_1 k_F^2} (1 + 4d^2 k_F^2). \quad (22)$$

Further, the thermoelectric conductivity could be found via $\alpha_{zz} = \sigma_{zz} S_{zz}$.

For the δ-form short-range scatters $d = 0$, $\sigma_{zz} \propto k_F^2$, and $S_{zz} \propto k_F^{-2}$, so the thermoelectric conductivity is a constant irrespective of the magnetic field

$$\alpha_{zz} = \frac{4\pi^2}{3} \frac{e k_B^2 T}{h} \frac{M_1}{V_G}. \quad (23)$$

It does not rely on carrier density or Fermi energy, indicating that α_{zz} attains plateaus under sufficiently strong magnetic fields. Previously observed in Dirac systems, the Hall thermoelectric conductivity demonstrates plateau behavior in the extreme quantum limit [23]. In this study, we identify the plateau characteristics of longitudinal thermoelectric conductivity. This phenomenon is expected to be applicable to all Weyl-like semimetals.

Now we move to the analysis of the screened Coulomb potential. The Fourier transform is $u(\boldsymbol{q}) = \frac{e^2}{\epsilon_0 \epsilon_r (q^2 + \kappa^2)}$ with ϵ_0 and ϵ_r being the dielectric constants of the vacuum and the material. The κ from the standard random phase approximation is $\kappa^2 = \frac{e^2}{2\pi \epsilon_0 \epsilon_r} \frac{1}{2\pi \ell_B^2} \frac{1}{M_1 k_F}$. In this case, the transport time is

$$\frac{\hbar}{\tau_{\text{tr}}^{0,C}} = \frac{V_C}{M_1 k_F} \frac{\ell_B^2}{8\pi} F_1(c_1). \quad (24)$$

Here $V_C = n_i e^4/(\epsilon_0^2 \epsilon_r^2)$, the function $F_1(x) = 1/x - e^x E_1(x)$ with $E_1(x) = \int_x^\infty dt\, e^{-t}/t$ being an exponential integral function, and $c_1 = (4k_F^2 + \kappa^2)\ell_B^2/2$. Therefore, the conductivity

has the form

$$\sigma_{zz} = \frac{e^2}{h} \frac{(4M_1 k_F)^2}{V_C \ell_B^4} \frac{1}{F_1(c_1)}, \quad (25)$$

meanwhile the Seebeck coefficient can be expressed as

$$S_{zz} = \frac{\pi^2 k_B^2 T}{3e} \frac{1}{M_1 k_F^2} \left[1 - \frac{k_F}{2} \frac{\partial \ln F_1(c_1)}{\partial k_F}\right]. \quad (26)$$

The function $F_1(x)$ has the following asymptotic behavior: $F_1(x) = 1/x$ when $x \ll 1$, while $F_1(x) = 1/x^2$ when $x \gg 1$. Hence, for $c_1 \ll 1$, $\sigma_{zz} \propto k_F^2 (4k_F^2 + \kappa^2)/\ell_B^2$, $S_{zz} \propto k_F^{-2}(16k_F^2 + \kappa^2)/(4k_F^2 + \kappa^2)$, and $\alpha_{zz} \propto (16k_F^2 + \kappa^2)/\ell_B^2$; while for $c_1 \gg 1$, we find $\sigma_{zz} \propto k_F^2 (4k_F^2 + \kappa^2)^2$, $S_{zz} \propto (4k_F^2 + \kappa^2)^{-1}$, $\alpha_{zz} \propto k_F^2 (4k_F^2 + \kappa^2)$. The κ relies on the Fermi wave vector k_F. Therefore, the magnetic field dependence of these three transport quantities strongly depends on how the Fermi wave vector relies on the field. It is known that k_F is related to the filling state of electrons. When the Fermi energy is fixed, the Fermi wave vector is given by

$$k_F = \sqrt{\frac{1}{M_1}(E_F + M_0 - \omega_c/2)}. \quad (27)$$

The B-dependence is in the frequency ω_c. Another choice is to keep the carrier density occupying the lowest energy band unchanged, that is to say $N_e = \sum_{k_x, k_z} \Theta(E_F - E_0)$ is a constant, which leads to

$$k_F = 2\pi^2 \ell_B^2 N_e. \quad (28)$$

Now the k_F is inversely proportional to the magnetic field.

Since the conductivity in the longitudinal configuration is the same as that of the two-node Weyl model, which has been carefully studied before [38,44], here we focus on the thermoelectric quantities of this coexisting model. Figure 3 shows the longitudinal thermoelectric transport contributions of the coexistence topological semimetal as a function of magnetic field at a fixed carrier density for the Gaussian-type [(a) and (c)] and Coulomb-type [(b) and (d)] elastic scatterings. For δ-form scattering ($d = 0$ in the Gaussian potential), the thermoelectric conductivity α_{zz} remains constant independent of the magnetic field, aligning with Eq. (23). However, for Gaussian-type scattering with nonzero distance, it linearly depends on the magnetic field at high field strengths. This behavior can be understood from Eqs. (21) and (22): for short distances, such as $dk_F \ll 1$, the thermoelectric conductivity exhibits a weak linear relationship with B, where $\alpha_{zz} = \sigma_{zz} S_{zz} \propto 1 + 2d^2/\ell_B^2$. For long distances (e.g., $d = 12$ nm), α_{zz} may first decrease and then increase with the increment of the field. At short distances where $dk_F \ll 1$, several curves ($d = 2, 4, 8$ nm) of the Seebeck coefficient almost exactly coincide and grow parabolically with the magnetic field since, in this case, $S_{zz} \simeq \frac{\pi^2 k_B^2 T}{3e} \frac{1}{M_1 k_F^2} \propto B^2$. As the distance increases, deviations begin to appear.

For the screened Coulomb scattering, we first discuss the results with large relative dielectric constant ($\epsilon_r = 20, 50$). The thermoelectric coefficient α_{zz} first decreases and then increases with the field shown in Fig. 3(b). For this case, the small field limit corresponds to $4k_F^2 \gg \kappa^2$, but the large field one corresponds to $4k_F^2 \ll \kappa^2$. We find the following:
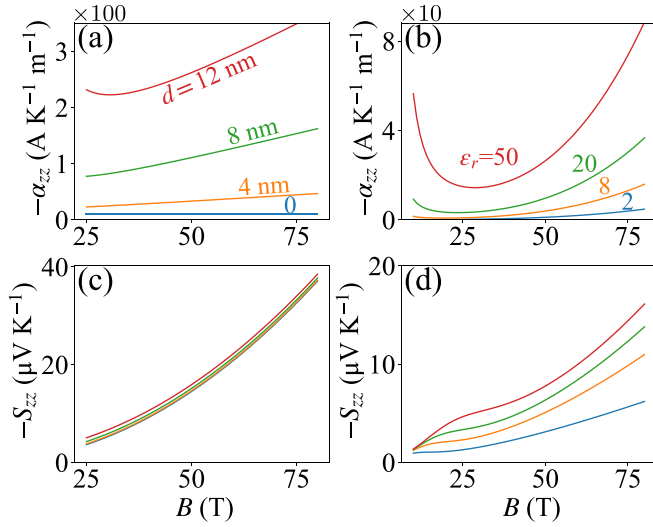
FIG. 3. The thermoelectric conductivity α_{zz} and the Seebeck coefficient of the coexisting system are plotted as functions of the magnetic field **B** at Gaussian [(a) and (c)] and Coulomb [(b) and (d)] potentials for fixed carrier density $N_e = 5 \times 10^{22}$ m^{-3}. The four curves in (a) and (c) are taken for $d = 0, 4, 8, 12$ nm, and four curves in (b) and (d) correspond to $\epsilon_r = 2, 8, 20, 50$. Here $V_G = 10^{-3}$ eV^2 nm^3, the impurity density for the screened Coulomb potential is taken as $n_i = 3 \times 10^{21}$ m^{-3}, and $T = 0.5$ K.

(i) In the small magnetic field limit, the thermoelectric coefficient α_{zz} transitions from $\propto B^{-4}$ at $2k_F^2 \ell_B^2 \gg 1$ to $\propto B^{-1}$ at $2k_F^2 \ell_B^2 \ll 1$, but S_{zz} is proportional to B^2 with the increment of the field according to the previous analysis. (ii) For the strong magnetic field limit, Eq. (26) can be simplified to $S_{zz} \simeq (2M_1 k_F^2)^{-1}(\ell_B^2 \kappa^2/2 + 1)^{-1}$ with the help of the approximation $F(c_1) \simeq 1/[c_1(c_1 + 1)]$. Hence, we find that S_{zz} transitions from $\propto B^2$ at $\ell_B^2 \kappa^2/2 \ll 1$ to $\propto B$ at $\ell_B^2 \kappa^2/2 \gg 1$ with the growth of the field indicating in Fig. 3(d). However, the thermoelectric coefficient $\alpha_{zz} = \sigma_{zz} S_{zz}$ is always proportional to B^3. Now we move to the low relative dielectric constant case ($\epsilon_r = 2, 8$). In this case, the strong screening condition ($4k_F^2 \ll \kappa^2$) is satisfied in the whole field regime. The smaller dielectric constants allow us to witness the linear growth of S_{zz} within smaller magnetic fields, as indicated by the orange and blue curves in Fig. 3(d). Similarly, α_{zz} maintains its cubic relationship with the magnetic field. Hence, the Gaussian or Coulomb scattering with a large dielectric constant is intentional for obtaining a large Seebeck coefficient.

At temperatures near 0 K, the chemical potential $\mu \approx E_F$. Alternatively, in experiments where a fixed Fermi energy is often considered, we select the Fermi energy $E_F = 2M_0$ to position the system in the quantum limit. Figure 4 depicts the variations of thermoelectric conductivity and Seebeck coefficients with magnetic field for two scattering potentials at a fixed Fermi energy. In this scenario, the magnetic field cannot be excessively applied, as a too-large magnetic field would elevate the lowest energy band E_0 beyond the Fermi energy, contrary to the fixed carrier density case. The results for Gaussian-type scattering are presented in (a) and (c). For δ-form scattering ($d = 0$), the thermoelectric coefficient α_{zz} remains constant. When the distance is nonzero
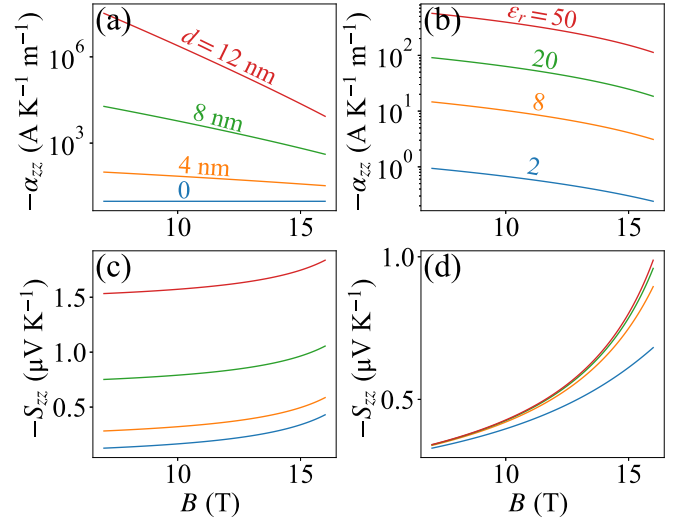

FIG. 4. The thermoelectric coefficients α_{zz} and the Seebeck coefficient of the coexisting system vs the magnetic field at Gaussian [(a) and (c)] and screened Coulomb [(b) and (d)] potentials at fixed Fermi energy $E_F = 2M_0$. The other parameters are the same as Fig. 3.

($d \neq 0$), α_{zz} increases rapidly with d and decreases swiftly with an increasing magnetic field due to the exponential relation $\alpha_{zz} \propto e^{4k_F^2 d^2}$. The Seebeck response S_{zz} increases with the field following $S_{zz} \propto k_F^{-2}$ for δ-form scattering. The curves of S_{zz} with $d \neq 0$ are essentially shifted by a field-independent constant $\frac{\pi^2 k_B^2 T}{3e} \frac{4d^2}{M_1}$ from the curve with $d = 0$, in accordance with Eq. (22). For screened Coulomb scattering, all thermoelectric conductivities with different ϵ_r decrease with the magnetic field. This decrement of α_{zz} for the fixed Fermi energy contrasts with the case of fixed carrier density. Regarding the Seebeck coefficient, where the dependence on ϵ_r only arises from κ, its value grows rapidly with the field, as shown in Fig. 4(d).

IV. TRANSVERSE CONFIGURATION

In the transverse configuration, the magnetic field remains aligned along the z-direction, maintaining the validity of the previously derived Landau energy bands and eigenstates. However, the electric field (temperature gradient) is now chosen to be along the x axis perpendicular to the magnetic field. In this way, the conductivities include the longitudinal one σ_{xx} and the Hall one σ_{xy}. For the longitudinal conductivity σ_{xx}, we could still use the Kubo formula. But the velocity should be taken as the component in the x direction. Since the z-direction magnetic field quantizes the energy in the x-y plane, the needed expectation value in the quantum limit $v_x = \langle \psi_0 | \hat{v}_x | \psi_0 \rangle$ is zero. Hence, the associated velocity elements come from the off-diagonal ones. The nonzero conductivity σ_{xx} originates from the interband velocity $v_{0,\pm 1} = \langle \psi_0 | \hat{v}_x | \psi_{\pm 1} \rangle$ [45]. $v_{0,+1}$ is expressed as

$$v_{0,+1} = \frac{1}{\hbar} \left(D k_z \sin \frac{\alpha_1}{2} + \frac{\sqrt{2}}{\ell_B} M_1 \cos \frac{\alpha_1}{2} \right). \quad (29)$$

$v_{0,-1}$ can be obtained by exchanging sine and cosine, as well as changing the sign from positive to negative in $v_{0,+1}$. The expression for the longitudinal conductivity in the quantum limit, σ_{xx}, is written as

$$\sigma_{xx} = \frac{\hbar e^2}{2\pi L_z} \frac{1}{2\pi \ell_B^2} \sum_{m=\pm 1, k_z} v_{0,m} G_m^A(E_F) v_{m,0} G_0^R(E_F), \quad (30)$$

where the retarded and advanced Green's functions at the Fermi energy are

$$G_0^R(E_F) = \frac{1}{E_F - E_0 + i\frac{\hbar}{2\tau_0}}, \quad (31)$$

$$G_{\pm 1}^A(E_F) = \frac{1}{E_F - E_{\pm 1} - i\frac{\hbar}{2\tau_{\pm 1}}}. \quad (32)$$

Here τ_0 and $\tau_{\pm 1}$ are the lifetimes, where $\tau_{\pm 1}$ describes the virtual process going back and forth between bands E_0 and $E_{\pm 1}$. We keep only the real part of σ_{xx} since the fields considered here are all static. In the weak scattering limit $E_F - E_m \gg \hbar/(2\tau_m)$, the conductivity σ_{xx} becomes

$$\sigma_{xx} \simeq \frac{\hbar e^2}{\pi L_z} \frac{1}{2\ell_B^2} \sum_{m,k_z} \left[\frac{\hbar}{2\tau_m} \frac{(v_{0,m})^2}{(E_F - E_m)^2} \delta(E_F - E_0) \right]. \quad (33)$$

The lifetime could be calculated in the Born approximation [42], where both the $k_z = k_F$ and $k_z = -k_F$ terms contribute in contrast to the transport time. Hence, they are given by

$$\frac{\hbar}{\tau_{\pm 1}} = \frac{n_i(1 \pm \cos\alpha_{1F})}{4M_1 k_F} \sum_{k_x'} \sum_{q_x, q_y} [|u(q_x, q_y, 0)|^2$$
$$+ |u(q_x, q_y, 2k_F)|^2] e^{-\zeta} \zeta \delta_{q_x, k_x - k_x'}, \quad (34)$$

with $\zeta = q_\parallel^2 \ell_B^2/2$. α_{1F} is the value of α_1 at $k_z = k_F$. The behavior of $\tau_{\pm 1}$ exhibits variance depending on the scattering potentials, leading to distinct transport quantities.

For the Gaussian potential, the relaxation time $\tau_{\pm 1}^G$ is given by a specific expression

$$\frac{\hbar}{\tau_{\pm 1}^G} = \frac{V_G \ell_B^2 (1 \pm \cos\alpha_{1F})}{8\pi M_1 k_F (2d^2 + \ell_B^2)^2} (1 + e^{-4k_F^2 d^2}). \quad (35)$$

Therefore, the corresponding σ_{xx} is of the form

$$\sigma_{xx}^G = \frac{e^2}{h} \frac{V_G \ell_B^2 (1 + \cos^2\alpha_{1F})}{64\pi^2 M_1^2 k_F^2 (2d^2 + \ell_B^2)^2} (1 + e^{-4k_F^2 d^2}). \quad (36)$$

The thermoelectric conductivity α_{xx} can be determined through the Mott relation $\alpha_{xx} = \frac{\pi^2 k_B^2 T}{3e} \frac{\partial \sigma_{xx}}{\partial E_F}$. It is worth noting that the material parameter D affects conductivity via the factor $1 + \cos^2\alpha_{1F}$. This factor only fluctuates between 1 and 2, hence its impact on the overall magnetic field dependence of conductivity is relatively minor. First, we disregard the influence of this factor. Additionally, when examining the magnetic field-dependent analytical behavior of transport quantities, we specifically consider the scenario of short-distance impurities, where $e^{-4d^2 k_F^2} \approx 1$. In the fixed carrier density situation, we find $\sigma_{xx}^G \propto B$ and $\alpha_{xx}^G \propto B^3$ for short magnetic length (large magnetic field) $2d^2 \gg \ell_B^2$, but $\sigma_{xx}^G \propto B^3$ and $\alpha_{xx}^G \propto B^5$ for long magnetic length (small magnetic field) $2d^2 \ll \ell_B^2$.

For the screened Coulomb potential, the lifetime becomes

$$\frac{\hbar}{\tau_{\pm 1}^C} = \frac{V_C \ell_B^2 (1 \pm \cos\alpha_{1F})}{16\pi M_1 k_F} [F_2(c_1) + F_2(c_2)], \quad (37)$$

with $c_2 = \ell_B^2 \kappa^2/2$. Hence, the conductivity σ_{xx}^C is expressed as

$$\sigma_{xx}^C = \frac{e^2}{h} \frac{V_C \ell_B^2 (1 + \cos^2\alpha_{1F})}{128\pi M_1^2 k_F^2} [F_2(c_1) + F_2(c_2)]. \quad (38)$$

We could also obtain α_{xx} from the Mott relation. Here the function $F_2(x) = -1 + (1 + x)e^x E_1(x)$. $F_2(x)$ exhibits the asymptotic behavior $F_2(x) \propto x^{-2}$ at $x \gg 1$, but $F_2(x) \approx \ln(1/x) - 1 - \gamma$ which is almost a constant independent of the magnetic field at $x \ll 1$ with γ being Euler's constant. For this screened Coulomb potential, we also neglect the effect of the factor $1 + \cos^2\alpha_{1F}$. We notice the following: (i) If $c_2 \gg 1$, the conductivity σ_{xx}^C is inversely proportional to the magnetic field at both strong screening ($4k_F^2 \ll \kappa^2$) and weak screening ($4k_F^2 \gg \kappa^2$) for the fixed carrier density case. (ii) However, if $c_2 \ll 1$, we have $\sigma_{xx}^C \propto B$ and $\alpha_{xx}^C \propto B^3$.

For this transverse configuration ($\boldsymbol{B} \parallel \hat{z}$ and $\boldsymbol{E} \parallel \hat{x}$), another important quantity is the Hall conductivity σ_{yx}. For this three-dimensional system dispersing with k_z, it is known that each k_z contributes a quantized Hall conductivity e^2/h, hence the total Hall conductivity is [45]

$$\sigma_{yx} = 2 \int_0^{k_F} \frac{dk_z}{2\pi} \frac{e^2}{h} = \frac{e^2}{h} \frac{k_F}{\pi}. \quad (39)$$

If we consider the case of the fixed carrier density N_e, we get the Hall conductivity at zero temperature $\sigma_{yx} = -eN_e/B$; this is the well-known classical Hall conductivity. Therefore, the resistivities ρ_{xx} and ρ_{xy} can be written as

$$\rho_{xx} = \frac{\sigma_{xx}}{\sigma_{xx}^2 + \sigma_{yx}^2}, \quad (40)$$

$$\rho_{xy} = -\rho_{yx} = \frac{\sigma_{yx}}{\sigma_{xx}^2 + \sigma_{yx}^2}. \quad (41)$$

In the presence of $\boldsymbol{B} \parallel \hat{z}$ and $-\nabla T \parallel \hat{x}$, due to the diffusion and drift motion of the carriers, the material generates voltage gradient, E_x and E_y, respectively, along the x and y directions. Therefore, the Seebeck and Nernst coefficients can be expressed as

$$S_{xx} = -E_x/|\nabla T| = \rho_{xx}\alpha_{xx} + \rho_{yx}\alpha_{xy}, \quad (42)$$

$$S_{xy} = E_y/|\nabla T| = \rho_{xx}\alpha_{xy} - \rho_{yx}\alpha_{xx}. \quad (43)$$

Here α_{xy} is a thermoelectric Hall coefficient, which in the quantum limit is given by [23,52]

$$\alpha_{xy}(B, T) = -\frac{e}{2\pi\hbar L_z} \sum_{k_z} s\left(\frac{E_0(k_z) - E_F}{k_B T} \right), \quad (44)$$

with the entropy per electron state being

$$s(x) = k_B \left[\ln(1 + e^x) - \frac{x}{1 + e^{-x}} \right]. \quad (45)$$

One should note that Eq. (44) is model-independent, which has been successfully applied to the Schrödinger particles [23,52], the Dirac semimetal [23], and the multi-Weyl semimetal [42]. If $M_1 k_F^2 = E_F - (-M_0 + \omega_c/2) \gg k_B T$, that
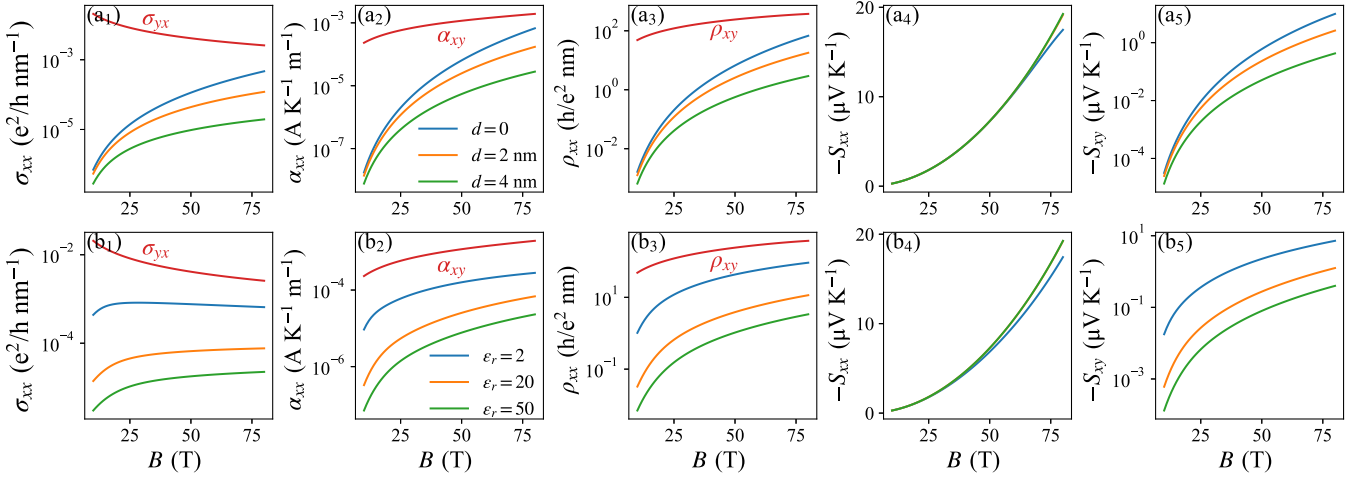
FIG. 5. The conductivities, thermoelectric conductivity α_{xx}, resistivities, Seebeck coefficient S_{xx}, and Nernst coefficient S_{xy} of the coexistence topological semimetals at fixed carrier density $N_e = 5 \times 10^{22}$ m^{-3} as functions of magnetic field under Gaussian (a$_1$, a$_2$, a$_3$, a$_4$, a$_5$) and screened Coulomb (b$_1$, b$_2$, b$_3$, b$_4$, b$_5$) scatterings in the transverse case. The red curves in (a$_1$), (a$_2$), and (a$_3$) [and (b$_1$), (b$_2$), and (b$_3$)] represent σ_{yx}, α_{xy}, and ρ_{xy}. Here $V_G = 10^{-3}$ eV^2 nm^3, the impurity concentration for the screened Coulomb potential is $n_i = 3 \times 10^{21}$ m^{-3}, and $T = 0.5$ K. The other model parameters are the same as in Fig. 2.

is to say, if the distance between Fermi energy and the bottom of the zeroth Landau band is much greater than $k_B T$, α_{xy} could be calculated as

$$\alpha_{xy} \simeq -\frac{ek_B^2 T}{24\hbar M_1 k_F} = \frac{e^2 k_B^2 T B}{48\pi^2 \hbar^2 M_1 N_e}. \tag{46}$$

It is proportional to the magnetic field when the carrier density is fixed, rather than a constant value, because the current lowest Landau level behaves like a Schrödinger particle [23].

Figure 5 shows the variation of σ_{xx}, α_{xx}, ρ_{xx}, S_{xx}, and S_{xy} with magnetic field at fixed carrier density for two scattering potentials [(a) Gaussian and (b) Coulomb potentials]. Additionally, employing Eqs. (39) and (44) yields σ_{yx} and α_{xy} displayed with red curves in the corresponding σ_{xx} and α_{xx}. For the δ-form scattering (blue curve), the longitudinal conductivity σ_{xx} experiences a faster increase than the cases with finite distances. This is due to $\sigma_{xx} \propto B^3$ under δ potential, while $\sigma_{xx} \propto B$ at large magnetic fields (short magnetic lengths) under Gaussian potential. Concerning the screened Coulomb potential, the conductivities increase with the magnetic field for both $\epsilon_r = 20$ and 50 in Fig. 5(b$_1$), whereas the conductivity for $\epsilon_r = 2$ (blue curve) initially increases and then decreases with the field. It is essential to note that logarithmic coordinates are used here, and a substantial decrease in conductivity is observable in normal coordinates [Fig. 6(c)]. The conductivity reduction is attributed to the fact that for small ϵ_r, $c_1 > c_2 \gg 1$ at large fields, causing the conductivity σ_{xx} to tend towards $\propto B^{-1}$. In Figs. 5(a$_2$) and 5(b$_2$), both longitudinal thermoelectric coefficients α_{xx} increase with the magnetic field. Contrary to the Dirac semimetal, the thermoelectric Hall conductivity α_{xy} exhibits an almost linear dependence on the field rather than forming a plateau, as seen by the red curves in Figs. 5(a$_2$) and 5(b$_2$). This behavior arises because the zeroth band of this semimetal is similar to the Schrödinger particle [23]. The large positive magnetoresistance takes place in Figs. 5(a$_3$) and 5(b$_3$) especially in the presence of Gaussian potential scattering. The Hall resistivity

linearly increases with the field, nearly independent of the scattering. Consequently, we only plot one curve in Figs. 5(a$_3$) and 5(b$_3$).

The Seebeck and Nernst coefficients for the two scattering potentials obtained through Eqs. (42) and (43) are shown in Figs. 5(a$_4$), 5(b$_4$), 5(a$_5$), and 5(b$_5$), respectively. In this configuration, the rapid growth of the Seebeck and Nernst coefficients is observed for both scatterings. For the Gaussian potential with small distance ($d = 2, 4$ nm) or the screened Coulomb potential with large dielectric constant ($\epsilon_r = 20, 50$), the Seebeck response can be approximated with the one in the dissipationless limit $S_{xx} \sim \alpha_{xy}/\sigma_{xy} \propto B^2$ inde-
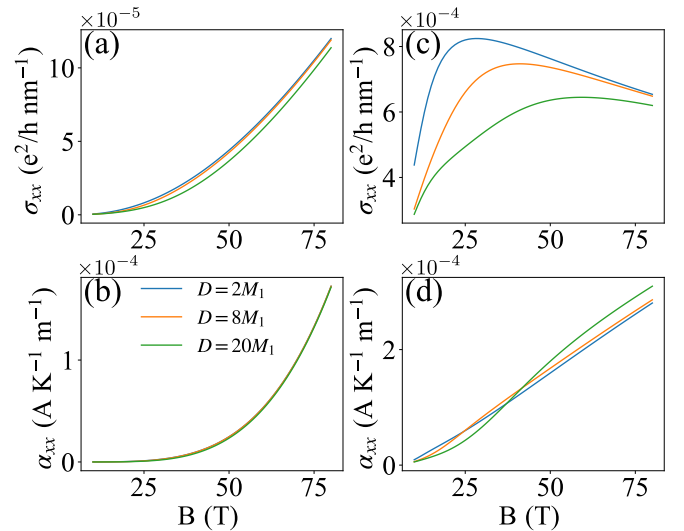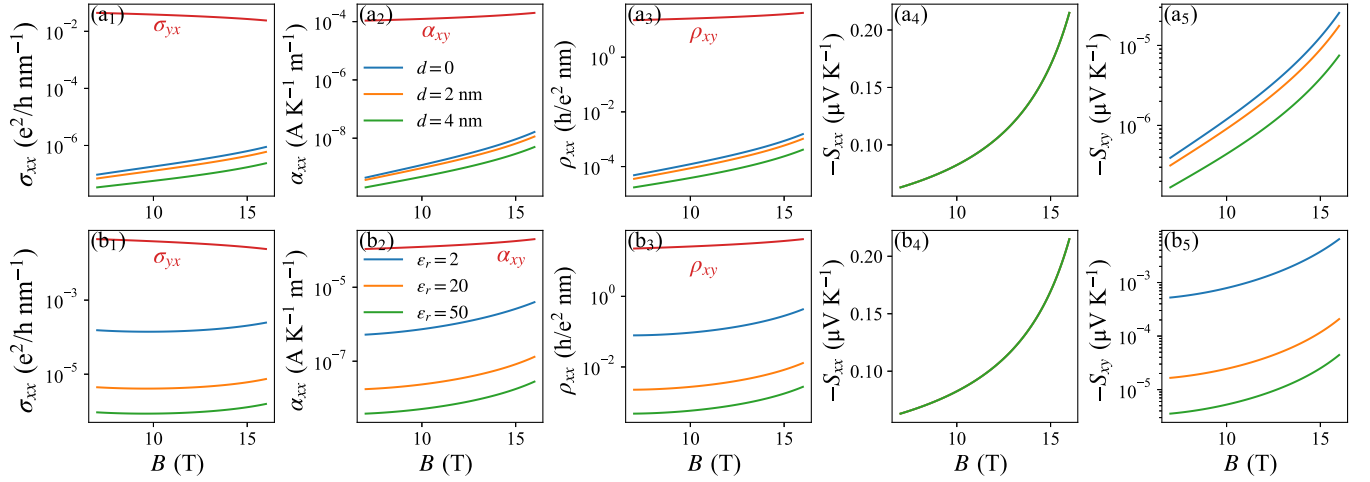

FIG. 6. The conductivities and thermoelectric conductivity α_{xx} of the transverse case as functions of magnetic field at fixed electron density $N_e = 5 \times 10^{22}$ m^{-3} for different $D = 2M_1, 8M_1, 20M_1$ under Gaussian [(a) and (b)] and screened Coulomb [(c) and (d)] scatterings. Here $d = 2$ nm and $\epsilon_r = 2$. The other parameters are the same as Fig. 5.

FIG. 7. Same as Fig. 5, but at fixed Fermi energy $E_F = 2M_0$.

pendent of the scattering. This parabolic behavior arises from the linear dependence of α_{xy}. In this scenario, $\sigma_{xx} \ll \sigma_{yx}$ at the given scattering parameters and electron density, making the first term in S_{xx} negligible. Hence, the yellow and green curves in S_{xx} almost completely overlap. The behavior of the S_{xx} is in sharp contrast to the Dirac/Weyl semimetal with a single node describing by the linear model $H \propto \boldsymbol{\sigma} \cdot \boldsymbol{k}$, where the Seebeck response exhibits a linear dependency on the field, attributed to the constant value of α_{xy} [22,23]. The S_{xx} of this coexisting system closely resembles that of Schrödinger particles [23], a similarity that stems from the fact that its lowest Landau band is also proportional to the square of k_z. In principle, S_{xx} of this system will also tend to saturate if the magnetic field reaches $2\pi^2 N_e \frac{\hbar}{|e|} \sqrt{\frac{M_1}{k_B T}}$. However, given that we are considering the low-temperature limit, the magnetic field required for saturation would far exceed 100 T. The Seebeck response deviates from the dissipationless limit for the δ-form scattering ($d = 0$) or the screened Coulomb scattering with small relative dielectric constant ($\epsilon_r = 2$) especially at larger magnetic field, where the $\rho_{xx}\alpha_{xx}$ in Eq. (42) contributes. In contrast, the behavior of the Nernst coefficient strongly depends on the scattering, as two larger quantities, α_{xy} and ρ_{yx}, are in the two parts of S_{xy}. It grows rapidly with the magnetic field, and the small distance d or the small dielectric constant ϵ_r could enhance its value.

The model parameter D distinguishes this coexistence model from the two-nodal Weyl model. In the transverse case, its effect will be revealed through the factor $\cos\alpha_{1F}$, which is illustrated in Fig. 6. We focus on the electric and thermoelectric conductivities for different scatterings [Gaussian scattering in (a) and (b), and screened Coulomb scattering in (c) and (d)]. It is observed that the effect of parameter D is mainly concentrated near a moderate magnetic field since $\cos\alpha_{1F}$ nearly equals the constant 0 or 1 at small (large) magnetic fields. For the Gaussian potential, the parameter D has a limited effect on the conductivity σ_{xx}, which slightly decreases with increasing D, and its magnetic field trend remains unchanged. However, the conductivity substantially decreases with increasing D for the screened Coulomb potential, and the trend changes slightly at the same time. Overall, the influence of the parameter D on thermoelectric conductivity α_{xx} is relatively small, as shown in Figs. 6(b) and 6(d).

The behaviors of these thermoelectric quantities at fixed Fermi energy are plotted in Fig. 7 (different scattering potentials) and Fig. 8 (effect of the model parameter D). For the Gaussian potential, we observe that σ_{xx} increases with the magnetic field, whereas it shows a slight decrease at fields less than 10 T for the screened Coulomb potential, in contrast to the case of fixed electron density. The Hall conductivity σ_{yx} exhibits a decreasing trend as the field increases. This trend stands in stark contrast to the one in Dirac semimetals with linear dispersion, where the Hall conductivity maintains a plateau value [24,53]. This phenomenon in Dirac semimetals can be attributed to the fact that the Fermi wave vector remains constant regardless of the magnetic field at fixed Fermi energy, as evident from Eq. (39), rendering the Hall conductivity independent of the magnetic field. Conversely, for this coexisting topological semimetal, Eq. (27) reveals that the Fermi wave vector is influenced by the magnetic field, thereby causing the Hall conductivity to vary with the magnetic field. The longitudinal thermoelectric conductivity α_{xx} grows with the magnetic field for both scatterings, as shown in Figs. 7(a_2) and 7(b_2). In the entire range of the magnetic field, $\sigma_{xx} \ll \sigma_{yx}$
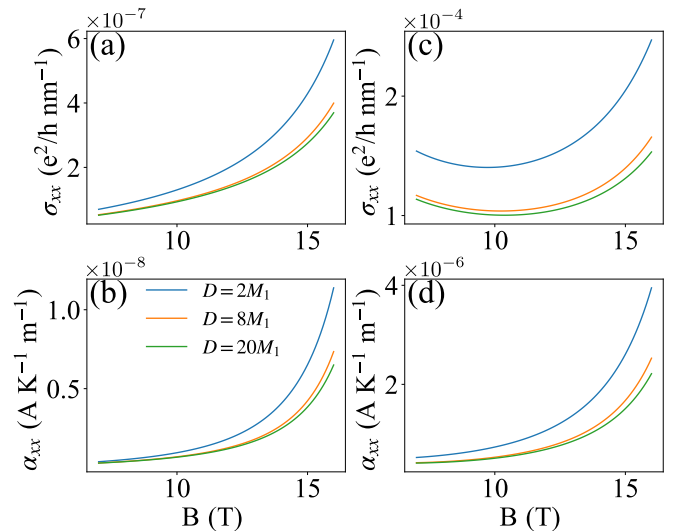
FIG. 8. Same as Fig. 6, but at fixed Fermi energy $E_F = 2M_0$.

holds, allowing the Seebeck coefficient to be approximated with the one of the dissipationless limit irrespective of the scattering, proportional to the square of the magnetic field. However, the Nernst response strongly depends on the type of scatterings. From Fig. 8, we can see that the model parameter D could rapidly diminish the conductivity and thermoelectric conductivity, though it does not change the variation tendency. For the two cases of fixed Fermi level and fixed electron density, the overall trend of these transport quantities is similar, but there are significant differences in the specific magnetic field-dependent behavior.

V. SUMMARY AND DISCUSSION

To conclude, we investigate the Landau bands of a coexisting topological system, and we discuss its thermoelectric transport properties in the quantum limit by using the linear-response theory. Such a system with coexisting Weyl points and nodal rings behaves like a Weyl semimetal for its zero Landau energy level and similarly to a nodal ring for its greater-than-zero Landau energy band. In the presence of two scattering potentials—a Gaussian potential and a screened Coulomb potential—we study the thermoelectric transport properties of the system, including both longitudinal and transverse configurations. The longitudinal configuration is the case when the magnetic field, temperature gradient, and electric field are all along the z-direction, while the transverse configuration chooses the magnetic field to remain along the z-direction while the electric field and temperature gradient are along the x-direction.

In the longitudinal configuration, the thermoelectric conductivity shows a plateau irrespective of the magnetic field and the Fermi energy for δ-form short-ranged scattering. For long-ranged Gaussian or screened Coulomb potentials, the thermoelectric coefficients strongly depend on the impurity distance or the relative dielectric constant. However, the Seebeck response always increases with the field for various scatterings at fixed carrier density or Fermi energy for longitudinal configuration. In the transverse configuration, significant positive magnetoresistance and enhanced thermoelectric conductance are observed for both Gaussian and screened Coulomb scatterings. The Hall conductivity surpasses the longitudinal conductivity, resulting in a Seebeck coefficient that approaches the dissipationless limit with a quadratic increase in the magnetic field, regardless of the nature of scattering. Conversely, the Nernst response exhibits a strong dependence on the specific scattering mechanism. Moreover, the thermoelectric transport properties are notably influenced by the model parameter D.

Beyond the theoretical predictions, recent experiments [54–56] have verified the topologically coexisting states in *real* materials, such as TaIrTe$_4$, PdBiSe, and LaSb$_2$, using angle-resolved photoemission spectroscopy and transport measurements. It is noteworthy, however, that these systems might exhibit greater complexity than the minimum coexistence model. In TaIrTe$_4$ [54], the topological coexistence state comprises 12 Weyl points and a pair of node lines protected by mirror symmetry. In PdBiSe, the coexistence state is composed of four distinct types of topological fermions, including Weyl, Rarita-Schwinger-Weyl, double

class-II three-component, and charge-2 fourfold fermions [55]. Additionally, LaSb$_2$ has been confirmed to possess both nodal lines and eightfold degenerate nodal points [56]. Among these materials, TaIrTe$_4$ appears to be closest to the theoretical model, as its coexisting state can be modulated by external strain, enabling the reduction of Weyl nodes to four. Recently, Jian *et al.* reported resistance and thermoelectric transport measurements in TaIrTe$_4$ [57]. The shift in chemical potential can result in transport properties being dominated by a single pocket in samples, corresponding to our single carrier case here. Unfortunately, there were no measurements of the thermoelectric power versus the magnetic field. We expect experimenters to conduct magnetic-field-dependent measurements of thermoelectric quantities in this material and, ultimately, to synthesize Cs$_2$MoCl$_6$-type ferromagnetic materials to directly test our theoretical predictions. Our work will also facilitate experimental progress in the thermoelectric measurement of other topologically coexisting materials.

APPENDIX: DERIVATION OF THE BERRY CURVATURE

Considering a general two-band model $H = d_0 + \boldsymbol{d} \cdot \boldsymbol{\sigma}$, where d_0 and $\boldsymbol{d} = (d_x, d_y, d_z)$ are functions of the wave vector, the energies of it are given by $E_\pm = d_0 \pm \sqrt{d_x^2 + d_y^2 + d_z^2}$. Here the symbols $\pm$ represent the conduction and valence bands, respectively. The Berry curvature of this general system for the conduction band is expressed as [58]

$$\Omega_+^\xi = -\epsilon_{\mu\nu\xi} \frac{(\partial_{k_\mu}\boldsymbol{d} \times \partial_{k_\nu}\boldsymbol{d}) \cdot \boldsymbol{d}}{2(d_x^2 + d_y^2 + d_z^2)^{3/2}}. \tag{A1}$$

Here $\epsilon_{\mu\nu\xi}$ is the Levi-Civita antisymmetric tensor with $\mu, \nu, \xi = (x, y, z)$.

For this coexistence semimetal, we find $d_0 = 0$, $d_x = Dk_zk_x$, $d_y = Dk_zk_y$, and $d_z = M_{\boldsymbol{k}}$. Therefore, the components of the Berry curvature for the conduction band are

$$\Omega_+^x = -\frac{1}{2E_+^3}\begin{vmatrix} \partial_{k_y}d_x & \partial_{k_y}d_y & \partial_{k_y}d_z \\ \partial_{k_z}d_x & \partial_{k_z}d_y & \partial_{k_z}d_z \\ d_x & d_y & d_z \end{vmatrix}$$
$$= \frac{D^2}{2E_+^3}k_zk_x\big[M_0 - M_1\big(k_x^2 + k_y^2 - k_z^2\big)\big], \tag{A2}$$

$$\Omega_+^y = \frac{1}{2E_+^3}\begin{vmatrix} \partial_{k_x}d_x & \partial_{k_x}d_y & \partial_{k_x}d_z \\ \partial_{k_z}d_x & \partial_{k_z}d_y & \partial_{k_z}d_z \\ d_x & d_y & d_z \end{vmatrix}$$
$$= \frac{D^2}{2E_+^3}k_zk_y\big[M_0 - M_1\big(k_x^2 + k_y^2 - k_z^2\big)\big], \tag{A3}$$

$$\Omega_+^z = -\frac{1}{2E_+^3}\begin{vmatrix} \partial_{k_x}d_x & \partial_{k_x}d_y & \partial_{k_x}d_z \\ \partial_{k_y}d_x & \partial_{k_y}d_y & \partial_{k_y}d_z \\ d_x & d_y & d_z \end{vmatrix}$$
$$= -\frac{D^2}{2E_+^3}k_z^2\big[M_0 + M_1\big(k_x^2 + k_y^2 - k_z^2\big)\big]. \tag{A4}$$

[1] X. Wan, A. M. Turner, A. Vishwanath, and S. Y. Savrasov, Topological semimetal and Fermi-arc surface states in the electronic structure of pyrochlore iridates, Phys. Rev. B **83**, 205101 (2011).

[2] G. Xu, H. M. Weng, Z. J. Wang, X. Dai, and Z. Fang, Chern semimetal and the quantized anomalous Hall effect in $HgCr_2Se_4$, Phys. Rev. Lett. **107**, 186806 (2011).

[3] A. A. Burkov and L. Balents, Weyl semimetal in a topological insulator multilayer, Phys. Rev. Lett. **107**, 127205 (2011).

[4] H. M. Weng, C. Fang, Z. Fang, B. A. Bernevig, and X. Dai, Weyl semimetal phase in noncentrosymmetric transition-metal monophosphides, Phys. Rev. X **5**, 011029 (2015).

[5] B. Q. Lv, H. M. Weng, B. B. Fu, X. P. Wang, H. Miao, J. Ma, P. Richard, X. C. Huang, L. X. Zhao, G. F. Chen, Z. Fang, X. Dai, T. Qian, and H. Ding, Experimental discovery of Weyl semimetal TaAs, Phys. Rev. X **5**, 031013 (2015).

[6] N. P. Armitage, E. J. Mele, and A. Vishwanath, Weyl and Dirac semimetals in three-dimensional solids, Rev. Mod. Phys. **90**, 015001 (2018).

[7] B. Q. Lv, T. Qian, and H. Ding, Experimental perspective on three-dimensional topological semimetals, Rev. Mod. Phys. **93**, 025002 (2021).

[8] A. A. Zyuzin and A. A. Burkov, Topological response in Weyl semimetals and the chiral anomaly, Phys. Rev. B **86**, 115133 (2012).

[9] V. Aji, Adler-Bell-Jackiw anomaly in Weyl semimetals: Application to pyrochlore iridates, Phys. Rev. B **85**, 241101(R) (2012).

[10] C. M. Wang, H.-Z. Lu, and S.-Q. Shen, Anomalous phase shift of quantum oscillations in 3D topological semimetals, Phys. Rev. Lett. **117**, 077201 (2016).

[11] C. M. Wang, H.-P. Sun, H.-Z. Lu, and X. C. Xie, 3D quantum hall effect of fermi arcs in topological semimetals, Phys. Rev. Lett. **119**, 136806 (2017).

[12] J. L. Zhang, C. M. Wang, C. Y. Guo, X. D. Zhu, Y. Zhang, J. Y. Yang, Y. Q. Wang, Z. Qu, L. Pi, H.-Z. Lu, and M. L. Tian, Anomalous thermoelectric effects of $ZrTe_5$ in and beyond the quantum limit, Phys. Rev. Lett. **123**, 196602 (2019).

[13] F. Xiong, C. Honerkamp, D. M. Kennes, and T. Nag, Understanding the three-dimensional quantum Hall effect in generic multi-Weyl semimetals, Phys. Rev. B **106**, 045424 (2022).

[14] T. Liang, Q. Gibson, J. Xiong, M. Hirschberger, S. P. Koduvayur, R. J. Cava, and N. P. Ong, Evidence for massive bulk Dirac fermions in $Pb_{1−x}Sn_xSe$ from Nernst and thermopower experiments, Nat. Commun. **4**, 2696 (2013).

[15] M. Hirschberger, S. Kushwaha, Z. Wang, Q. Gibson, S. Liang, C. A. Belvin, B. A. Bernevig, R. J. Cava, and N. P. Ong, The chiral anomaly and thermopower of Weyl fermions in the half-heusler GdPtBi, Nat. Mater. **15**, 1161 (2016).

[16] Z. Jia, C. Li, X. Li, J. Shi, Z. Liao, D. Yu, and X. Wu, Thermoelectric signature of the chiral anomaly in Cd_3As_2, Nat. Commun. **7**, 13013 (2016).

[17] T. Liang, J. Lin, Q. Gibson, T. Gao, M. Hirschberger, M. Liu, R. J. Cava, and N. P. Ong, Anomalous nernst effect in the dirac semimetal Cd_3As_2, Phys. Rev. Lett. **118**, 136601 (2017).

[18] M. Matusiak, J. Cooper, and D. Kaczorowski, Thermoelectric quantum oscillations in ZrSiS, Nat. Commun. **8**, 15219 (2017).

[19] C.-L. Zhang, T. Liang, M. Bahramy, N. Ogawa, V. Kocsis, K. Ueda, Y. Kaneko, M. Kriener, and Y. Tokura, Berry curvature generation detected by Nernst responses in ferroelectric

[20] Weyl semimetal, Proc. Natl. Acad. Sci. USA **118**, e2111855118 (2021).

[20] M. S. Alam, A. Fakhredine, M. Ahmad, P. K. Tanwar, H.-Y. Yang, F. Tafti, G. Cuono, R. Islam, B. Singh, A. Lynnyk, C. Autieri, and M. Matusiak, Sign change of anomalous Hall effect and anomalous Nernst effect in the Weyl semimetal CeAlSi, Phys. Rev. B **107**, 085102 (2023).

[21] H. Zhang, C. Q. Xu, and X. Ke, Topological Nernst effect, anomalous Nernst effect, and anomalous thermal Hall effect in the Dirac semimetal Fe_3Sn_2, Phys. Rev. B **103**, L201101 (2021).

[22] B. Skinner and L. Fu, Large, nonsaturating thermopower in a quantizing magnetic field, Sci. Adv. **4**, eaat2621 (2018).

[23] V. Kozii, B. Skinner, and L. Fu, Thermoelectric Hall conductivity and figure of merit in Dirac/Weyl materials, Phys. Rev. B **99**, 155123 (2019).

[24] F. R. Pratama, R. Saito, and N. T. Hung, Magneto-Seebeck coefficient of the Fermi liquid in three-dimensional Dirac and Weyl semimetals, Phys. Rev. B **106**, L081304 (2022).

[25] W. Zhang, P. Wang, B. Skinner, R. Bi, V. Kozii, C.-W. Cho, R. Zhong, J. Schneeloch, D. Yu, G. Gu, L. Fu, X. Wu, and L. Zhang, Observation of a thermoelectric Hall plateau in the extreme quantum limit, Nat. Commun. **11**, 1046 (2020).

[26] P. Wang, C. W. Cho, F. Tang, P. Wang, W. Zhang, M. He, G. Gu, X. Wu, Y. Shao, and L. Zhang, Giant Nernst effect and field-enhanced transversal z_NT in $ZrTe_5$, Phys. Rev. B **103**, 045203 (2021).

[27] F. Han, N. Andrejevic, T. Nguyen, V. Kozii, Q. T. Nguyen, T. Hogan, Z. Ding, R. Pablo-Pedro, S. Parjan, B. Skinner, A. Alatas, E. Alp, S. Chi, J. Fernandez-Baca, S. Huang, L. Fu, and M. Li, Quantized thermoelectric Hall effect induces giant power factor in a topological semimetal, Nat. Commun. **11**, 6167 (2020).

[28] A. Kiswandhi, T. Ochi, T. Taen, M. Sato, K. Uchida, and T. Osada, Quantized thermoelectric Hall plateau in the quantum limit of graphite as a nodal-line semimetal, Phys. Rev. B **107**, 195106 (2023).

[29] T. Osada, T. Ochi, and T. Taen, Thermoelectric Hall effect at high-magnetic-field quantum limit in graphite as a nodal-line semimetal, J. Phys. Soc. Jpn. **91**, 063701 (2022).

[30] X. Zhao, P. J. Guo, F. Ma, and Z.-Y. Lu, Coexistence of topological Weyl and nodal-ring states in ferromagnetic and ferrimagnetic double perovskites, Phys. Rev. B **103**, 085138 (2021).

[31] T. Zhang, D. Hara, and S. Murakami, Unique surface-state connection between Weyl and nodal ring fermions in ferromagnetic material Cs_2MoCl_6, Phys. Rev. Res. **3**, L042037 (2021).

[32] M. Li, J. Song, and Y. Jiang, Coexistence of topological type-II Weyl and triply degenerate points in a chiral photonic metamaterial, Phys. Rev. B **105**, 085304 (2022).

[33] J. Wu, S. Ke, Y. Guo, H. Zhang, and H. Lü, Weyl nodes and hybrid nodal loop with spin–orbit coupling in W_2TeSe, Appl. Phys. Lett. **123**, 193101 (2023).

[34] J. Zhan, J. Li, W. Shi, X.-Q. Chen, and Y. Sun, Coexistence of Weyl semimetal and Weyl nodal loop semimetal phases in a collinear antiferromagnet, Phys. Rev. B **107**, 224402 (2023).

[35] V. Saini, B. Patra, B. Singh, and A. Thamizhavel, Coexistence of phononic Weyl, nodal line, and threefold excitations in

chalcopyrite $CdGeAs_2$ and associated thermoelectric properties, arXiv:2301.00635.

[36] G. Chang, S.-Y. Xu, and H. Zheng, Room-temperature magnetic topological Weyl fermion and nodal line semimetal states in half-metallic heusler Co_2TiX (X=Si, Ge, or Sn), Sci. Rep. **6**, 38839 (2016).

[37] J.-P. Sun, D. Zhang, and K. Chang, Coexistence of topological nodal lines, Weyl points, and triply degenerate points in TaS, Phys. Rev. B **96**, 045121 (2017).

[38] S.-B. Zhang, H.-Z. Lu, and S.-Q. Shen, Linear magnetoconductivity in an intrinsic topological Weyl semimetal, New J. Phys. **18**, 053039 (2016).

[39] X.-T. Ji, H.-Z. Lu, Z.-G. Zhu, and G. Su, Competition between the inter-valley scattering and the intra-valley scattering on magnetoconductivity induced by screened Coulomb disorder in Weyl semimetals, AIP Adv. **7**, 105003 (2017).

[40] V. Könye and M. Ogata, Thermoelectric transport coefficients of a Dirac electron gas in high magnetic fields, Phys. Rev. B **100**, 155430 (2019).

[41] L. Feng, T. Ma, and Y. Zheng, Magneto-conductivity of Weyl semimetals: the roles of inter-valley scattering and high-order Feynman diagrams, J. Phys.: Condens. Matter **32**, 205502 (2020).

[42] L. X. Fu and C. M. Wang, Thermoelectric transport of multi-Weyl semimetals in the quantum limit, Phys. Rev. B **105**, 035201 (2022).

[43] Y. Li, H. Wang, J. Wang, C. Wang, Y. Liu, J. Ge, J. Niu, W. Zhang, P. Wang, R. Bi, J. Zhang, J.-Y. Dai, J. Yan, D. Mandrus, N. Samarth, H. Lu, X. Wu, and J. Wang, Anomalous magnetothermoelectric behavior in massive Dirac materials, Phys. Rev. B **107**, 085140 (2023).

[44] S. Li, H.-Z. Lu, and X. C. Xie, Impurity and dispersion effects on the linear magnetoresistance in the quantum limit, Phys. Rev. B **107**, 235202 (2023).

[45] H. Z. Lu, S. B. Zhang, and S. Q. Shen, High-field magnetoconductivity of topological semimetals with short-range potential, Phys. Rev. B **92**, 045203 (2015).

[46] C. Li, C. M. Wang, B. Wan, X. Wan, H.-Z. Lu, and X. C. Xie, Rules for phase shifts of quantum oscillations in topological nodal-line semimetals, Phys. Rev. Lett. **120**, 146602 (2018).

[47] C. M. Wang, H.-Z. Lu, and X. C. Xie, Quantum oscillation beyond the quantum limit in pseudospin Dirac materials, Phys. Rev. B **102**, 041204(R) (2020).

[48] Y. Ferreiros, A. A. Zyuzin, and J. H. Bardarson, Anomalous Nernst and thermal Hall effects in tilted Weyl semimetals, Phys. Rev. B **96**, 115202 (2017).

[49] M. Jonson and G. D. Mahan, Mott's formula for the thermopower and the Wiedemann-Franz law, Phys. Rev. B **21**, 4223 (1980).

[50] R. Lundgren, P. Laurell, and G. A. Fiete, Thermoelectric properties of Weyl and Dirac semimetals, Phys. Rev. B **90**, 165115 (2014).

[51] G. D. Mahan, *Many-Particle Physics* (Plenum, New York, 1990).

[52] D. L. Bergman and V. Oganesyan, Theory of dissipationless nernst effects, Phys. Rev. Lett. **104**, 066601 (2010).

[53] F. Tang, Y. Ren, P. Wang, R. Zhong, J. Schneeloch, S. A. Yang, K. Yang, P. A. Lee, G. Gu, Z. Qiao, and L. Zhang, Three-dimensional quantum Hall effect and metal-insulator transition in $ZrTe_5$, Nature (London) **569**, 537 (2019).

[54] X. Zhou, Q. Liu, Q. S. Wu, T. Nummy, H. Li, J. Griffith, S. Parham, J. Waugh, E. Emmanouilidou, B. Shen, O. V. Yazyev, N. Ni, and D. Dessau, Coexistence of tunable Weyl points and topological nodal lines in ternary transition-metal telluride $TaIrTe_4$, Phys. Rev. B **97**, 241102(R) (2018).

[55] B. Q. Lv, Z.-L. Feng, J.-Z. Zhao, N. F. Q. Yuan, A. Zong, K. F. Luo, R. Yu, Y.-B. Huang, V. N. Strocov, A. Chikina, A. A. Soluyanov, N. Gedik, Y.-G. Shi, T. Qian, and H. Ding, Observation of multiple types of topological fermions in PdBiSe, Phys. Rev. B **99**, 241104(R) (2019).

[56] Y. Qiao, F. Wang, H. Wang, Z. Tao, Z. Jiang, Z. Liu, S. Cho, F. Zhang, Q. Meng, W. Xia, Y. Yang, Z. Huang, J. Liu, Z. Liu, Z. Zhu, S. Qiao, Y. Guo, H. Zhang, and D. Shen, Experimental observation of multiple topological nodal structure in $LaSb_2$, Sci. China Phys. Mech. Astron. **67**, 247411 (2024).

[57] Y. Jian, Q. Wu, M. Yang, Q. Feng, J. Duan, D. Chen, Q. Wang, W. Xiao, Y. Shi, O. V. Yazyev, and Y. Yao, Transport signatures of temperature-induced chemical potential shift and Lifshitz transition in layered type-II Weyl semimetal $TaIrTe_4$, 2D Mater. **8**, 015020 (2021).

[58] X.-L. Qi, Y.-S. Wu, and S.-C. Zhang, Topological quantization of the spin Hall effect in two-dimensional paramagnetic semiconductors, Phys. Rev. B **74**, 085308 (2006).